Materials and Design 195 (2020) 109056

Contents lists available at ScienceDirect

Materials and Design

journal homepage: www.elsevier.com/locate/matdes

Investigation of metal mixing in laser keyhole welding of dissimilar metals

Wenkang Huang [a], Hongliang Wang [b,*], Teresa Rinker [b], Wenda Tan [a,*]

[a] Department of Mechanical Engineering, University of Utah, Salt Lake City, UT 84112, USA
[b] Manufacturing Systems Research Laboratory, Global Research and Development, General Motors LLC, Warren, MI 48092, USA

HIGHLIGHTS

- The underlying physics of metal mixing in laser welding of dissimilar metals are investigated.
- The chemical concentration field and metal mixing pattern are characterized by EDS element mapping.
- The effects of recoil pressure and Marangoni force on fluid flow and metal mixing are studied.
- The effects of welding parameters on the metal mixing are studied.

GRAPHICAL ABSTRACT

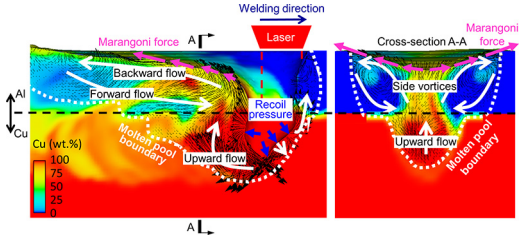

ARTICLE INFO

Article history:
Received 20 June 2020
Received in revised form 6 August 2020
Accepted 10 August 2020
Available online 13 August 2020

Keywords:
Laser welding
Dissimilar metals
Metal mixing
Fluid flow
Computational fluid dynamics

ABSTRACT

Laser keyhole welding of dissimilar metals has broad applications in various industrial fields. However, dissimilar metal mixing in the molten pool often causes the formation of detrimental intermetallic compounds that can undermine the performances of the dissimilar metal joints. In this study, the metal mixing process in laser keyhole welding of dissimilar metals is investigated with a combination of experimental and modeling approaches. The parametric experimental study is conducted to reveal the effects of laser power, welding speed, and heat input on the metal mixing in the fusion zone. *Ex-situ* energy-dispersive X-ray spectroscopy element mapping is used to characterize the metal mixing status in the fusion zone. To investigate the underlying physics of the welding process, a numerical model is developed to simulate the heat transfer, fluid flow, and metal mixing in the molten pool. It is found that the recoil pressure contributes to an upward flow that pushes copper to migrate from the bottom of the molten pool to the top. Meanwhile, the Marangoni force generates one backward flow and two side vortices that facilitate the metal mixing. An increase of laser power increases both the recoil pressure and the Marangoni stress, which drives more copper to migrate upward and mix with aluminum. An increase of welding speed reduces the molten pool lifetime, which reduces the metal mixing by the fluid flow. The investigation of dissimilar metal redistribution provides insights regarding the formation of intermetallic compounds in the joints, which is valuable for the design and optimization of the welding process in different industries.

1. Introduction

Dissimilar metal welding has been widely utilized in various industries, such as construction, automotive, aerospace, and electronics, where different materials provide advantages due to their specific material properties [1–3]. Joining these dissimilar metals using a robust method then becomes very important. Laser welding can be performed at a high welding speed

* Corresponding authors.
E-mail addresses: hongliang.wang@gm.com (H. Wang), wenda.tan@mech.utah.edu (W. Tan).

https://doi.org/10.1016/j.matdes.2020.109056

which significantly increases the throughput, and hence has been considered as a promising joining process for dissimilar metals. However, a critical challenge for laser welding (as well as all other fusion welding processes) of dissimilar metals is the formation of intermetallic compounds (IMCs). As dissimilar metals are melted in the molten pool, they can mix to form IMCs during solidification [4–7]. IMCs are usually brittle materials with reduced electrical conductance, which can remarkably undermine the mechanical and electrical performances of dissimilar metal joints [8–10].

Numerous experiments have been carried out on the dissimilar metal welding using both standard [11–17] and modified [18–26] laser welding processes. For the standard laser welding process, most of the reported work was focused on investigating the effects of different welding parameters on the IMCs formation in the fusion zone, microstructure of joint materials, and mechanical properties of the joints [11–15]. Only limited efforts were taken to understand the metal mixing in the welds [16,17]. Fortunato et al. [16] compared the metal mixing results in the molten pool for lap joints of Aluminum (Al)-on-Copper (Cu) and Cu-on-Al configurations. Similar vortex mixing patterns were observed in the Al-rich region for both stack-ups. Shamsolhodaei et al. [17] investigated the element distribution in the laser welding of butt joints between Nickel (Ni) alloy and Cu. When the laser was focused on the joint centerline, the final joint had a homogeneous element distribution. When the laser was offset from the joint centerline by 50 μm toward the Cu side, an uneven mixing was observed in the final joint. It was speculated that the offset altered the temperature distribution, which further affected the fluid flow and metal mixing in the molten pool.

In the modified laser welding of dissimilar metals, features such as laser beam oscillation [18–20], ultrasonic vibration [21–23], or external magnetic fields [24–26], are implemented. These techniques can alter the fluid flow and metal mixing in the molten pool. Kraetzsch et al. [19] found that when the laser beam oscillation frequency was fixed at 2500 Hz, a homogeneously mixed fusion zone could be produced with the laser beam oscillation at amplitudes of 0.9 mm and 0.4 mm for lap joint and butt joint configurations, respectively. It was speculated that the additional laser beam oscillation led to severer keyhole fluctuation that accelerated the fluid flow and extended the molten pool lifetime, both of which facilitated metal mixing in the molten pool. Zhou et al. [22] showed that for laser welding of a Ni alloy and stainless steel, the distribution of Ni in the fusion zone changed from uneven to even when the ultrasonic vibration power acting on the welding platform was increased from 0 W to 500 W. It was speculated that the cavitation and acoustic streaming effects caused by the ultrasonic vibration generated high-intensity turbulent flows in the molten pool to accelerate the mixing of dissimilar metal elements. Yan et al. [24] found that by applying a steady magnetic field of 120 mT in laser welding of steel and Al alloy, the average thickness of the IMCs layer was increased up to 25 μm. It was speculated that the magnetic field facilitated iron diffusion into Al.

While all these experiments have successfully revealed the effects of different factors on the metal mixing, the fundamental physics that govern the mixing process are not clearly understood. All the theoretical explanations regarding dynamic phenomena during the welding process are usually speculations based on the *ex-situ* characterization of the joint microstructure. Since it is still technically challenging to perform *in-situ* investigations on the dynamic metal mixing during laser welding, Computational Fluid Dynamics (CFD) simulation offers another approach to assist the understanding of this important issue.

Extensive efforts have been made in the modeling of laser welding of dissimilar metals. However, most reported work was focused on conduction mode laser welding. These modeling studies can be divided into two categories based on the specific fluid problems that they targeted: laminar flow models and turbulent flow models.

For the laminar flow models, some early modeling works from Phanikumar et al. [27,28] studied the heat transfer and fluid flow in the molten pool and their effects on the metal mixing in laser welding of butt joints between Ni and Cu. The results showed that the molten pool geometry was asymmetric due to the difference of thermal properties between the two metals. As the molten pool developed, the Ni side was melted earlier and experienced more convection and mixing. In a recent work, Hu et al. [29] conducted similar work on laser welding between stainless steel and Ni in the butt joint configuration. The results also showed the asymmetric temperature field and molten pool geometry due to the different thermal properties between the two metals. Because of the insufficient molten pool lifetime for metal mixing at the early stage of melting, iron was unevenly distributed in the fusion zone. Esfahani et al. [30] investigated the mixing of two engineering alloys (instead of pure element metals), i.e., low carbon steel and stainless steel in laser welded butt joints. They concluded that the molten pool dynamics, surface topology, and alloy mixture were significantly influenced by the temperature gradient and surface tension of the molten pool. Xue et al. [31] studied the metal mixing of Cu and Al in the lap joint configuration. Their modeling results indicated that the diffusion of the two metals was the main mechanism that formed the composition transition layer in the fusion zone.

In the turbulent flow models, additional turbulence equations or the modification of material properties (e.g., mass diffusivity, thermal conductivity, and viscosity) due to the turbulent flow effect need to be considered [32,33]. Chakraborty et al. [34,35] studied the metal mixing process with special attention to the inclusion of additional turbulence equations in the model. The turbulent flow model predicted a more uniform concentration field of the two metals than the laminar flow model. Moreover, the turbulent flow model predictions agreed well with the experimental results, while the laminar flow model showed a 10 wt% underestimation of the Ni concentration.

While these modeling studies have revealed the Marangoni force as being the dominating driving force for the fluid flow and metal mixing in the conduction mode laser welding of dissimilar metals, the dominating mechanisms in the keyhole mode laser welding can be drastically different. There has been evidence from both experiments [36–38] and simulations [38–41] to demonstrate that the unstable keyhole fluctuation in the laser keyhole welding of single metals can significantly alter the fluid flow in the molten pool. Similar effects should be expected for keyhole welding of dissimilar metals. Substantial work has been reported to investigate the keyhole dynamic, fluid flow in the molten pool, thermal history, and mechanical properties of welds [42–46]. However, only a few models investigated dissimilar metal mixing in the molten pool. Isaev et al. [47] built a 3D numerical model for laser keyhole welding of titanium and stainless steel with an intermediate Cu insert. The fluid flow and the metal mixing were not explicitly calculated in the model, and the possible locations for metal melting and mixing were only speculated upon the temperature field. Tomashchuk et al. [48] used the COMSOL software to build a simplified 2D model for laser keyhole welding of butt joints between steel and Cu. They found that a zero laser offset from the centerline of the joint provided more evident metal mixing in the molten pool. However, the model used a predefined circular moving keyhole, and the effects of dynamic keyhole fluctuation on the fluid flow and metal mixing were not considered. Wu et al. [49] developed a 3D model using the Fluent software for laser keyhole welding of lap joints between stainless steel and titanium. Heat transfer, fluid flow, keyhole wall evolution, and solute diffusion between dissimilar metals were simulated in this model. Since the model only considered diffusion but neglected advection, only a diffusion layer could be observed at the interface between the two metals instead of a mixing layer due to the fluid flow. Tan and Huang developed a 3D model to investigate the effect of thermo-fluid flow on the metal mixing process in laser keyhole welding of lap joints of Ni and Cu [50], but the predictions were not validated against the experiments.

In this work, both experiments and simulations are used to study the underlying physics of metal mixing in laser keyhole welding of dissimilar metals in the lap joint configuration. A parametric study is conducted to identify the effects of different welding parameters on the metal mixing in the fusion zone. A CFD model is developed to reveal the underlying physics of the metal mixing process by predicting the heat transfer, fluid flow, and metal mixing in the molten pool. The effects of different welding parameters on the spatial distributions of laser absorption, temperature, driving forces, fluid flow, and metal mixing in the molten pool are quantitatively analyzed based on the modeling results. By combining the experimental and modeling results, the underlying physics of the metal mixing process in laser keyhole welding of dissimilar metals are revealed.

2. Experiment setup

Fig. 1 shows the lap joint configuration for the experiments. Al and Cu are selected due to their broad applications in various batteries. An AA1100 Al plate of 0.2 mm thickness is placed on top of a nearly pure Cu (C10100) plate of 0.5 mm thickness. Irradiation of the stack-up is performed with a fiber laser with a maximum power output of 2000 W at the wavelength of 1070 nm. The laser beam is delivered by an optical fiber with a dimension of 50 μm in diameter before connecting to a galvo scanner, which results in a minimum spot size of approximately 115 μm at the focal plane. The working distance of the scan head is 300 mm and the scanning area with the f-theta lens is 125 mm by 125 mm. The laser is focused along the normal direction of the top surface of the Al plate and moves linearly to perform line scan welding. Shielding gas is not used in the experiment because the shielding gas flow will create an external mechanical impact on the molten pool surface that may change the fluid flow and metal mixing in the molten pool.

In order to investigate the effects of different welding parameters on the metal mixing process, multiple joint samples are produced with different welding parameters, as shown in Table 1. Six cases in the parametric matrix are selected for further analyses. The three cases in the top row, i.e., #1, #2, and #3, have identical welding speed but different laser powers. The three cases in the right column, i.e., #3, #5, and #6, have identical laser power but different welding speeds. The three cases in the matrix diagonal, i.e., #1, #4, and #6, have identical heat input (3340 J/m, defined as laser power divided by welding speed) but different laser powers and welding speeds.

After welding, the joints are cut along their cross-sections and polish the cut surfaces. An optical microscope is used to observe the geometry of the fusion zone cross-sections. Energy-dispersive X-ray spectroscopy (EDS) element mapping is used to characterize the Cu concentration field in the cross-sections, whichcan reflect the metal mixing situation in the molten pool.

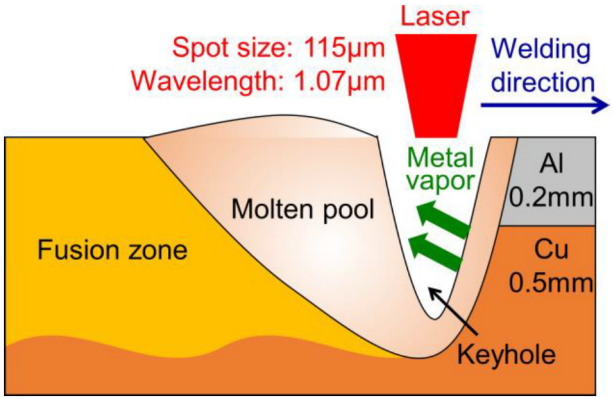

Fig. 1. Experiment setup of laser keyhole welding for Al–Cu lap joints.

Table 1
Experimental parameters.

	668 W	922 W	1170 W
0.2 m/s	#1	#2	#3
0.276 m/s		#4	#5
0.35 m/s			#6

3. Model description

A 3D numerical model is developed using the Flow-3D® software. The calculation domain of the model is shown in Fig. 2. This calculation domain represents a small subset of the experimental coupons and welding region. The coupon thickness for the material is the same for the model as in the experiment.

The calculation domain is divided into uniform meshes. A mesh convergence test is carried out by using five different mesh sizes (25 μm, 20 μm, 15 μm, 10 μm, and 5 μm) to run the simulation for case #6. The time step is set accordingly to ensure that the Courant–Friedrichs–Lewy (CFL) number is less than 0.5 for the simulations. The total mesh numbers for the five mesh sizes are 1.92×10^5, 3.75×10^5, 8.98×10^5, 3×10^6, and 2.4×10^7, and the corresponding calculation times are 0.17 h, 0.8 h, 3 h, 18 h, and 312 h on a 20-core machine with Intel Xenon CPU 2.30 GHz and 192 GB RAM. The maximum temperature and maximum velocity in the molten pool are chosen as the criteria for the convergence. As shown in Fig. 3, mesh independent solutions of the maximum temperature and maximum velocity have been achieved with a mesh size of <10 μm. Therefore, a mesh size of 10 μm is chosen in this study.

As Fig. 2 shows, boundary conditions are imposed on the calculation domain to approximate conditions in the experiment. Since the top and the bottom parts of the calculation domain are air, the boundary conditions are set to be the constant pressure (atmospheric pressure) boundary condition. The four sides of the calculation domain are set to be the outflow boundary condition.

3.1. Fluid flow and metal mixing

The fluid flow determines the metal mixing process in the molten pool. In this model, the velocity field, temperature field, and Cu concentration field are all calculated for the solid and liquid phases with the following governing equations.

$$\frac{\partial}{\partial t}(\rho) + \nabla\left(\rho \vec{V}\right) = 0 \tag{1}$$

$$\frac{\partial}{\partial t}\left(\rho \vec{V}\right) + \nabla\left(\rho \vec{V}\vec{V}\right) = \nabla\left(\mu \nabla \vec{V}\right) - \nabla P - \frac{\mu}{K}\vec{V} + \rho g \tag{2}$$

$$\frac{\partial}{\partial t}(\rho h) + \nabla\left(\rho \vec{V} h\right) = \nabla(k \nabla T) \tag{3}$$

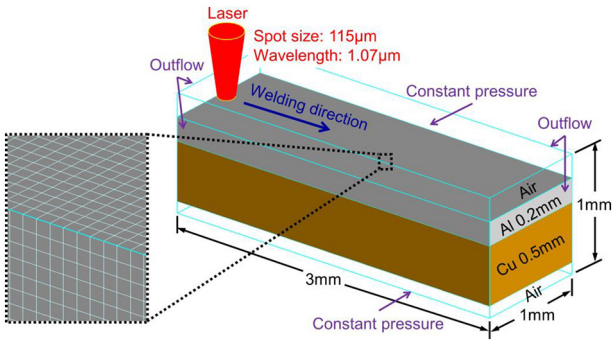

Fig. 2. Model setup and calculation domain.

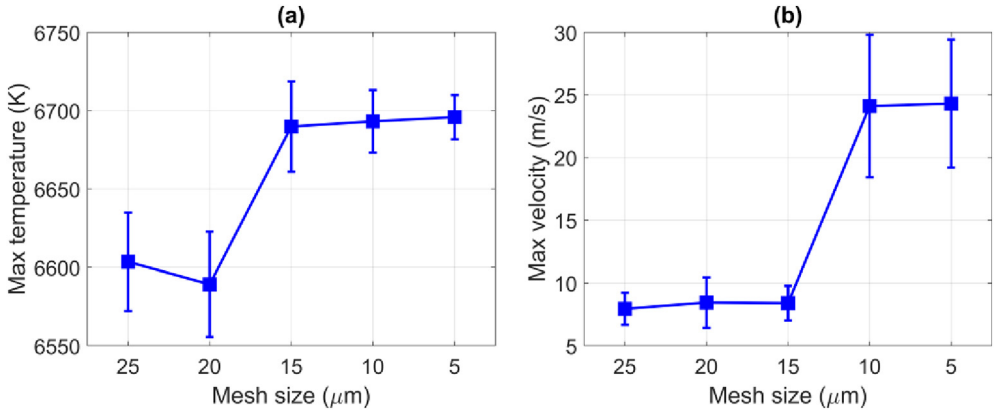

Fig. 3. Mesh convergence test.

$$\frac{\partial}{\partial t}(\rho Y) + \nabla\left(\rho \vec{V} Y\right) = \nabla(D\rho\nabla Y) \tag{4}$$

In the mass conservation equation (Eq. (1)), ρ is the density of the fluid, and $\vec{V}$ is the fluid velocity. In the momentum conservation equation (Eq. (2)), μ is the fluid viscosity, P is the pressure, K is the isotropic permeability expressed by the Kozeny-Carman equation, and g is the gravity. The last two terms on the right-hand side of Eq. (2) are the source terms that represent the damping force for the liquid phase and the gravitational force, respectively. In the energy conservation equation (Eq. (3)), T is the temperature, h is the material enthalpy, and k is the thermal conductivity. In the species conservation equation (Eq. (4)), Y is the Cu concentration in weight percentage, and D is the mass diffusivity. The thermal properties of Al and Cu used in this work are temperature dependent and are listed in Table 2 [51–54].

3.2. Keyhole formation and evolution

The Volume-Of-Fluid (VOF) method [55–58] is employed to track the evolution of interface (including the molten pool surface and keyhole wall). Eq. (5) shows the governing equation of VOF.

$$\frac{\partial f}{\partial t} + \nabla\left(f \cdot \vec{V}\right) = 0 \tag{5}$$

Here f is the fraction of liquid volume over cell volume and $\vec{V}$ is the fluid velocity obtained from the solution from Eq. (1) and Eq. (2). The VOF method defines f=1 in the cells of liquid or solid, f=0 in the cells of gas, and 1>f>0 in the cells on the interface. By solving Eq. (5), the distribution of f will be updated, and the interface appears in the cells with 1>f>0.

There are three major forces on the interface. The first is the recoil pressure caused by metal evaporation, which can be calculated with Eq. (6) [59].

$$P_{\text{recoil}} = \alpha P_v \cdot \exp\left[\frac{\Delta H_v}{(\gamma_v - 1)c_v T_v}\left(1 - \frac{T_v}{T}\right)\right] \tag{6}$$

Here α is the evaporation coefficient, P_v is the evaporation pressure, ΔH_v is the latent heat of evaporation, γ_v is the heat capacity ratio of metal vapor, c_v is the specific heat of metal vapor, T_v is the evaporation temperature, and T is the temperature at the keyhole wall. The direction of the recoil pressure is along the normal direction of the keyhole wall and points toward the liquid side. The second force is the Laplace pressure P_L, which is caused by the surface tension on a curved interface as calculated by Eq. (7).

$$P_L = \gamma\kappa \tag{7}$$

Table 2
Thermal properties of Al and Cu as a function of temperature T(K) at solid (s) and liquid (l) states.

Property	Al	Cu
ρ (kg/m^3)	$-4.99 \times 10^{-4}\ T^2 + 0.322\ T + 2648$ (s) $-0.299\ T + 2670$ (l)	8960 (s) $-0.807\ T + 9072$ (l)
k (W/m·K)	$-0.067\ T + 248$ (s) $-2.099 \times 10^{-5}\ T^2 + 7.892 \times 10^{-2}\ T + 33.9$ (l)	7.509×10^{-2} T + 418.8 (s) $4.976 \times 10^{-2}\ T + 89.7$ (l)
c_p (J/kg·K)	1199 (s) 1127 (l)	385 (s) 572 (l)
γ (mN/m)	$-0.127\ T + 993$ (l)	$-0.176\ T + 1552$ (l)
μ (mPa·s)	$10^{(-0.7324+803.49/T)}$ (l)	$10^{(-0.4220+1393.4/T)}$ (l)
T_m (K)	933	1358
T_v (K)	2743	2835

Here γ and κ are the surface tension and interface curvature, respectively. γ is a function of temperature T and Cu concentration Y. The third force is the Marangoni force caused by the gradient of surface tension on the interface. The spatial variations of temperature and Cu concentration on the interface cause a gradient of the surface tension. The surface tension gradient caused by the temperature gradient is the thermo-capillary stress, which has been included in the majority of laser keyhole welding models. The surface tension gradient caused by the Cu concentration gradient is the soluto-capillary stress, which has barely been mentioned in the existing literature. The thermo-capillary stress and the soluto-capillary stress altogether forms the Marangoni stress σ_M which can be calculated by Eq. (8).

$$\sigma_M = \nabla_s \gamma \tag{8}$$

Here ∇_s calculates the gradient along the tangent direction of the interface.

3.3. Laser-material interaction

The laser experiences multiple-reflections in laser keyhole welding, so the ray-tracing model is used to model this phenomenon [38,60–62]. This method divides the laser beam into multiple rays. Each ray has a specific size, direction, and power. Then the multiple reflection route of each ray is explicitly tracked based on the law of reflection. For each incidence, the absorbed laser power equals the power of the incident ray multiplied by the absorption rate. The absorption rate is defined as the percentage of laser power that can be absorbed by the materials. It depends on the laser wavelength, incident angle, material, and temperature. In this work, the build-in ray-tracing function in Flow-3D® is used to predict the laser absorption

in the keyhole. The absorption rates of Al and Cu are calculated as temperature-dependent [63].

4. Result and discussion

4.1. Experimental results

The molten pool geometry (white dashed curve) and Cu concentration field (color map) for the six cases can be found in the EDS element mapping results in Fig. 4.

It is found that the molten pool geometry changes significantly with the welding parameters. The general molten pool geometry shows a larger width on the Al side than that on the Cu side for all six cases. Three geometric descriptors are defined for the molten pool to better investigate the changes to the molten pool based on welding parameters (shown in Fig. 5(a)): the maximum molten pool width on the Al side (denoted by Width1), the molten pool width at the interface of Al and Cu (denoted by Width2), and the molten pool depth on the Cu side (denoted by Depth). The geometry descriptors as functions of the laser power and welding speed are shown in Fig. 5. With a fixed welding speed, the molten pool dimensions increase with an increasing laser power, as shown in Fig. 5(b). With a fixed laser power, the molten pool dimensions increase with a decreasing welding speed, as shown in Fig. 5(c). These two trends can be easily explained by a heat input calculation: an increase in laser power or a decrease in welding speed will increase the heat input, which leads to a wider and deeper molten pool. With the heat input fixed in cases #1, #4, and #6, the molten pool dimensions slightly increase from case #1 with the "low" parameter combination (i.e., low laser power and welding speed) to case #6 with the "high" parameter combination (i.e., high laser power and welding speed), as shown in Fig. 5(d). This is because the time available for the heat to be dissipated away from the laser heating spot is shorter in #6 due to the high welding speed. A higher percentage of the absorbed laser power will be utilized locally to melt the metal.

It is also found that Al and Cu have been redistributed during welding, but they are not completely mixed over the entire molten pool. Two regions of very different concentrations are formed in the molten pool with a sharp boundary between them. The top region (denoted as Region I hereafter) has all the Al coming from the top Al plate, but a reasonable amount of Cu has flowed up from the bottom Cu plate and is mixed well with Al. The bottom region (denoted as Region II hereafter) is dominated by the pre-existing Cu in the bottom plate, but a minor amount of Al has flowed down from the top Al plate and is well mixed with Cu.

To quantify the amount of Cu that flows to the top region from the bottom Cu plate, the average Cu concentration in Region I is calculated from the EDS element mapping results and shown as a function of the welding parameters in Fig. 5(e). For cases #1, #2, and #3 with a fixed welding speed, the average Cu concentration in Region I increases with the increasing laser power. For cases #3, #5, and #6 with a fixed laser power, the average Cu concentration in Region I increases with a decreasing welding speed. Different metal mixing patterns can also be observed from the experimental results. For case #1, #4, and #6 with a fixed heat input but increasing laser power and welding speed, the high laser power and high welding speed scenario (case #6) is more likely to form vortex mixing patterns in Region I. While the low laser power and low welding speed scenario (case #1) has a uniformly distributed mixing in Region I.

Cracks are found in the fusion zones in cases #2, #3 and case #5, in which the average Cu concentration in Region I is above 50 wt%. According to the Al—Cu phase diagram, IMCs of Al_2Cu, AlCu, Al_3Cu_4, and Al_4Cu_9 are likely to form with the Cu concentration of >50 wt% [8,9]. These brittle IMCs may have caused the cracks in the fusion zone as indicated with the black arrows in Fig. 4.

4.2. Simulation results and discussion

4.2.1. Model validation

The model has been applied to simulate all the cases listed in Table 1. Modeling results are validated by comparing their molten pool geometries and Cu concentration fields against the experimental results. The modeling results of all cases agree reasonably well with the experimental results. Two typical cases (#1, 668 W at 0.2 m/s; and #6, 1170 W at 0.35 m/s) are selected to show the validation results, as given in Fig. 6. The predicted molten pool geometries are compared with the optical microscope image results side-by-side. The predicted

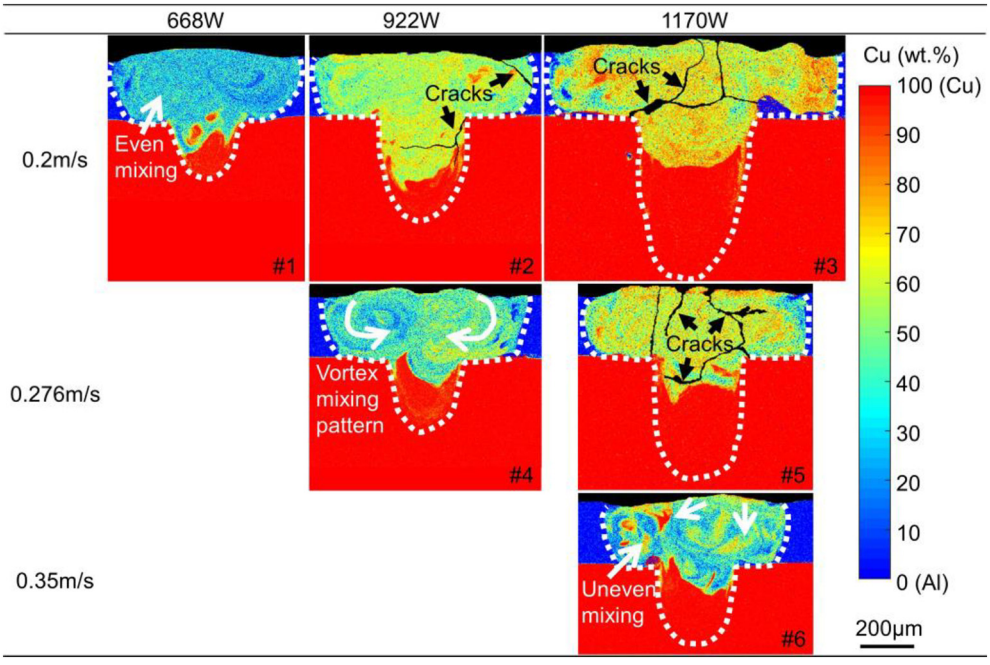

Fig. 4. Experimental results of EDS element mapping of the molten pool geometry (white dashed curve), Cu concentration field (color map), cracking locations (black arrows), and mixing patterns (white arrows) in the cross-section view of the molten pool for six cases.

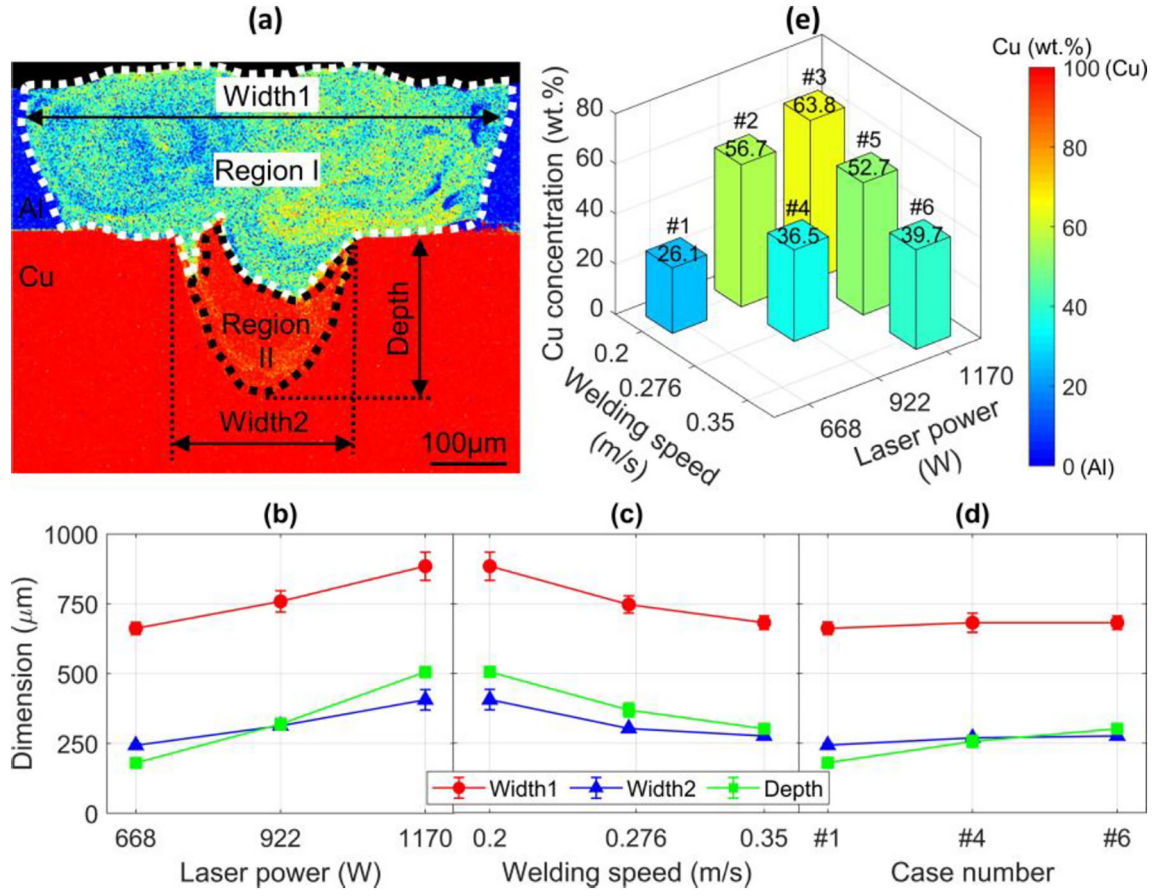

Fig. 5. Experimental results of the Cu concentration of joint cross-section of case #4, (a) showing the definition of geometric descriptors. Geometric descriptors are shown as functions of laser power, welding speed, and different parameter combinations of the same heat input for (b–d) respectively. The average Cu concentration in Region I is shown for six cases (e).

Cu concentration fields are compared with the EDS element mapping results side-by-side. For a more quantitative comparison, EDS element line scanning is conducted along a horizontal line (AA') at the middle of the Region I and a vertical line (BB') at the center of the molten pool.

4.2.2. Metal mixing process

To illustrate the physics for the metal mixing process, the modeling result of case #6 is presented below. Four snapshots of the welding process are given in Fig. 7. For better visual effects of the molten pool, keyhole dynamic, and metal mixing process, the calculation domain is sliced along the center plane of the welding direction (i.e., longitudinal direction). Fig. 7(a) shows that the keyhole has fully penetrated the top Al plate and starts to penetrate the bottom Cu plate. This indicates the initial stage of the metal mixing process where the melted Cu at the bottom begins to move upward. Fig. 7(b) shows that the keyhole has just entered the quasi-steady state and the Cu has started to mix with the Al in Region I. Fig. 7(c) shows the stage where the keyhole and molten pool geometries and the metal mixing pattern have both reached quasi-steady states. The Cu element distribution is still evolving in the liquid molten pool but is already fixed in the solidified fusion zone. Eventually, Fig. 7(d) shows the redistributed dissimilar metal elements in the entire fusion zone after the welding process is completed. A crater and a pore are formed at the end of the weld.

A further investigation is then focused on the physics regarding the metal mixing in the quasi-steady state. The simulation results at 3.29 ms for case #6 (i.e., Fig. 7(c)) are shown in Fig. 8 to study the quasi-steady state, and the following observations can be made.

- The laser absorption is critical to the entire welding process. The distribution of the laser heat flux in the keyhole is shown in Fig. 8(a). The black dashed line is the initial boundary of the Al plate and the Cu plate. Due to the multiple reflections of the laser rays inside the keyhole, the majority of the laser power has been deposited on the keyhole bottom as well as the lower portion of the rear keyhole wall.
- The laser heat flux determines the temperature distribution on the keyhole wall and in the molten pool. As shown in Fig. 8(b), the high-temperature area is mainly at the bottom keyhole wall due to the highest laser heat flux in the area. Also, a temperature gradient can be observed at the molten pool surface: a higher temperature is found in the area with a higher laser heat flux, and the temperature is lower in the area with a lower laser heat flux.
- The temperature distribution on the keyhole wall determines the driving forces for the fluid flow in the molten pool. Fig. 8(b) shows the driving forces and the projected fluid velocity field, with the fluid velocity vector (both direction and speed) visualized by the black arrows. First, the high temperature at the keyhole bottom generates a recoil pressure of megapascal magnitude to push the fluid away from the keyhole bottom. This flow will be deflected by the molten pool boundary and then flow upward. It is denoted as the upward flow in the following discussion. Second, the temperature gradient at the molten pool surface generates a Marangoni force that drives the fluid on the molten pool surface to move from the high-temperature areas to the low-temperature areas, i.e., backward to the molten pool tail. This flow is denoted as the backward flow in the following discussion. Finally, once the liquid arrives at the molten pool tail, it will turn around and move forward to the keyhole

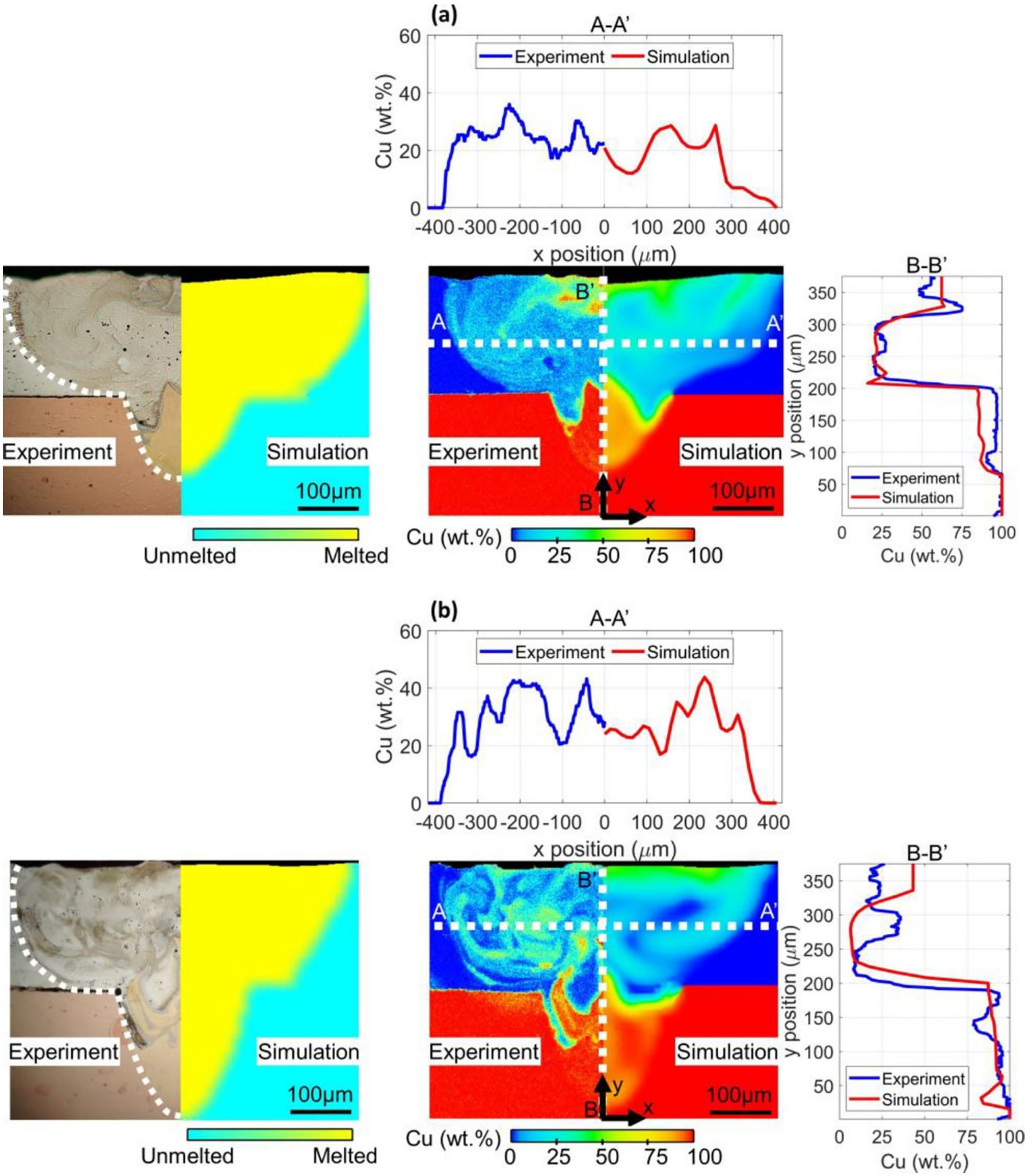

Fig. 6. Comparison of the experimental and modeling results of the molten pool geometry and Cu concentration field for (a) case #1 and (b) case #6.

again. This is denoted as the forward flow in the following discussion. The backward flow and forward flow collaboratively form a vortex on the center plane.

- Eventually, the fluid flow determines the metal mixing in the molten pool. Fig. 8(c) shows the Cu concentration distribution at the center plane of the molten pool as a result of the fluid flow. Cu at the molten pool bottom migrates with the upward flow into Region I of the molten pool. Once it gets close to the top surface of the molten pool, it will flow along the backward-forward vortex to mix with the Al in Region I.

The predicted distribution of Cu concentration on the center plane of the joint is shown in Fig. 9(a) and matches reasonably well with the

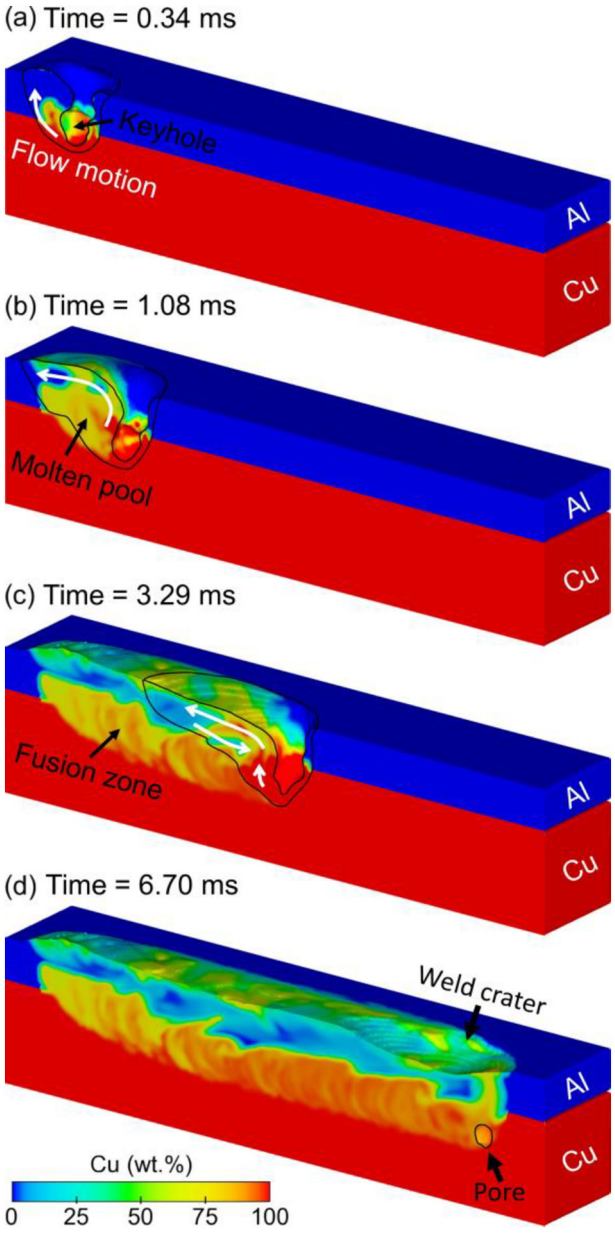

Fig. 7. Snapshots of Cu concentration fields at different moments of simulation for case #6.

experimental results in Fig. 9(b). Specifically, the prediction is consistent with the experimental result in the following two aspects:

- Bands of high and low concentrations (as marked out by the white dashed curves) are generated alternatively in the solidified region. The model reveals that the banded distribution of concentration is caused by the unstable fluctuation of the keyhole. While the general fluid flow and metal mixing pattern in the molten pool have been described in Fig. 8, the keyhole fluctuation can change the laser heat flux, temperature, and recoil pressure at the keyhole bottom, and hence change the fluid velocity (particularly the upward flow). When there is a surge of high-speed flow in the molten pool, the whole flow pattern enables a more effective mixing of the two metals, generating a higher Cu concentration in Region I of the molten pool and a higher Al concentration (i.e., a lower Cu concentration) in Region II. As the mixed metals solidify at the tail edge of the molten pool, a band of high Cu concentration will be "locked" in Region I of the solidified region, and a band of low Cu concentration will be "locked" in Region II of the solidified region. The bands are well aligned with the solidification front (i.e., the molten pool boundary) of the moment. Similarly, when there is a surge of slow flow in the molten pool, bands of low Cu concentration and low Al concentration will be "locked" in Regions I and II of the solidified regions, respectively.
- Some Cu-rich clusters (as marked out by the red dashed circles) can be found in Region I of the solidified region. These Cu-rich clusters indicate the insufficient mixing of Al and Cu at certain locations during the welding process. The model reveals the formation process of these clusters. When Cu flows into Region I and moves toward the molten pool surface or the molten pool boundary, some Cu-rich fluid clusters solidify rapidly (due to the high thermal conductivity of Cu) before they break up to mix with Al. Therefore, these Cu-rich clusters are typically located close to the molten pool surface and molten pool boundary.

While Fig. 8(c) shows the projected fluid flow in the center plane of the molten pool, three locations, labeled by "A", "B", and "C", have been marked out in Fig. 8(c), and the driving forces and resultant projected fluid flow on these three cross-sections from the simulation are shown in Fig. 10. The following observations can be made from the cross-sectional analyses.

- Section A is located on the keyhole center. As shown in Fig. 10(a), the recoil pressure is the dominating driving force and it pushes the fluid away from the keyhole bottom. Besides, the Marangoni force contributes to the vortex flow on both sides of the molten pool.
- Section B is located behind the rear keyhole wall. As shown in Fig. 10(b), an upward flow is observed in the center region of this section to drive the Cu into Region I. This flow is the upward flow in Fig. 8(b). In the meantime, the Marangoni force dominates on the molten pool surface to drive the vortex flow on both sides of the molten pool. The two vortices drive the upward-flowing Cu to go sideways and mix with Al.
- Section C is located close to the tail of the molten pool. As shown in Fig. 10(c), there are still two flow vortices on the two sides of the molten pool, which is driven by the Marangoni force. The force is smaller than that on section B because the local temperature gradient is much lower.

It is noted that the flow vortices on the two sides of the molten pool near its top surface have been found on all the three cross-sections. These vortices are consistent with the Al—Cu mixing vortices on the joint cross-sections revealed by the EDS element mapping results in Fig. 4.

4.2.3. Effects of welding parameters on metal mixing

While a qualitative introduction of the physics is already given in Section 4.2.2 for case #6, more quantitative analyses will be performed in this section. The values of all variables of interest will be obtained for each case from their simulations, and the dependency on the processing parameters will be determined. This analysis will reveal the effects of welding parameters on the fluid flow and metal mixing in the process.

Fig. 11 presents a series of data to investigate the effects of welding parameters on the migration of Cu. The migration of Cu is primarily driven by the upward flow shown in Fig. 8(b). The amount of Cu that flows upward is quantified by the average Cu concentration in Region I.

The effects of laser power on the Cu migration are shown in column (a) of Fig. 11. The welding speed is fixed at 0.2 m/s in cases #1, #2, and #3, while the laser power is increased from 668 W to 922 W and 1170 W. As a result, the maximum laser heat fluxes on the keyhole wall are 4.5×10^{10} W/m^2, 6×10^{10} W/m^2, and 6.5×10^{10} W/m^2 for the three cases, and the maximum temperature on the keyhole wall increases from 5900 K to 6350 K and 6500 K. The maximum recoil

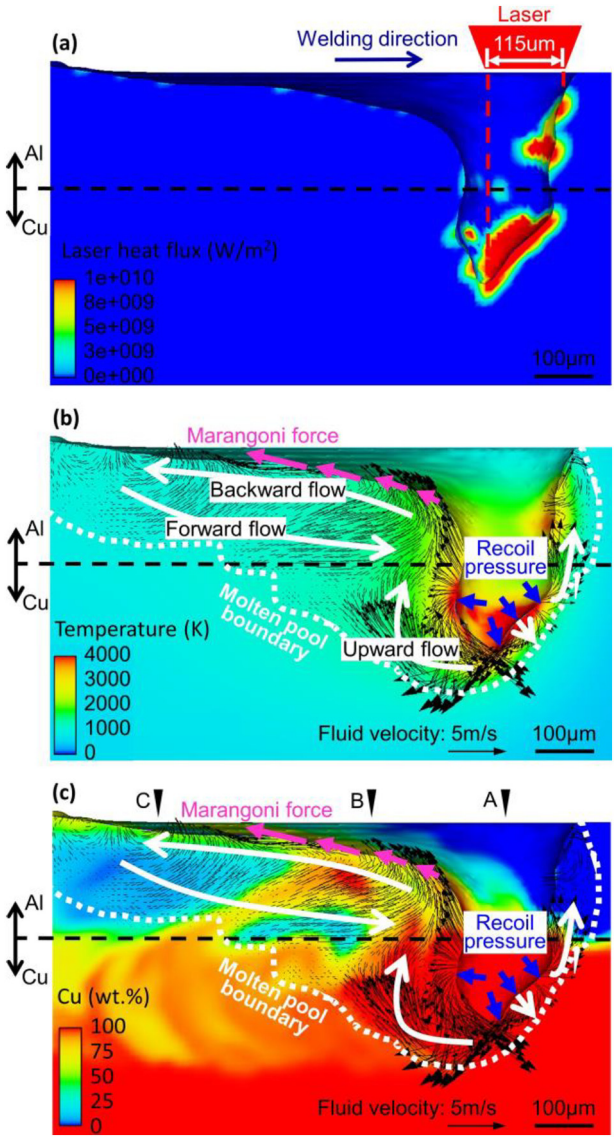

Fig. 8. Simulation results of the longitudinal section views of (a) laser heat flux field, (b) temperature and fluid velocity fields, and (c) Cu concentration field for case #6.

pressure on the keyhole wall are 1.05×10^6 Pa, 1.25×10^6 Pa, and 1.33×10^6 Pa, respectively. The increasing recoil pressure in the three cases drives the fluid flow to accelerate, with the maximum fluid velocity being 9 m/s, 11.2 m/s, and 12.5 m/s, respectively. An increase in the fluid velocity can drive more Cu to flow upward, and thus the average Cu concentration in Region I increases from 28 wt % to 47 wt% and 55 wt% in the three cases.

The effects of welding speed are shown in column (b) of Fig. 11. The laser power is fixed at 1170 W in cases #3, #5, and #6, while the welding speed is increased from 0.2 m/s to 0.276 m/s and 0.35 m/s. The maximum laser heat flux, maximum temperature, and maximum recoil pressure on the keyhole wall are very similar in all the three cases due to the identical laser power, but the maximum fluid velocity decreases from 12.5 m/s to 10.9 m/s and 8.7 m/s. This is because the increase of welding speed allows less time for one region to be heated by the laser, and hence less time is available for the local fluid to be accelerated by the laser-induced recoil pressure. As a result, the maximum fluid velocity and the average Cu concentration in Region I are reduced in the three cases.

The effects of different parameter combinations for the same heat input are shown in column (c) of Fig. 11. The heat input is fixed at 3340 J/m for cases #1, #4, and #6, while the welding parameters are changed from a "low" combination to "medium" and "high". As the laser power is increased, the maximum laser heat flux, maximum temperature, and maximum recoil pressure also increase in the three cases. As the welding speed is increased, the fluid in one region has less time to absorb heat from the laser and accelerate due to the recoil pressure. The conflicting effects of the increasing recoil pressure and the decreased acceleration time result in the maximum fluid velocities in the three cases being very similar, i.e., around 9 m/s, as thus similar average Cu concentrations in Region I are found for the three cases as well, i.e., around 30 wt%.

Once Cu enters Region I, it will mix with the pre-existing Al in the region. It is mentioned in the discussion of Fig. 10 that the Marangoni force is the major reason for the mixing, and here a more quantitative analysis is presented in Fig. 12.

The effects of laser power on the Al—Cu mixing are shown in column (a) of Fig. 12. When the welding speed is fixed at 0.2 m/s and the laser power is increased from 668 W to 1170 W, the maximum Marangoni stress is increased from 4.2×10^4 N/m^2 to 5.8×10^4 N/m^2 and 7.0×10^4 N/m^2. Driven by the Marangoni force, the maximum fluid velocity on the molten pool surface increases from 2.05 m/s to 2.25 m/s and 2.63 m/s. In the meantime, the molten pool lifetime increases from 2.8 ms to 3.8 ms and 4.2 ms due to the increased laser power. Both the increased surface fluid velocity and elongated molten pool lifetime can improve the Al—Cu mixing, so the standard deviation of Cu concentration in Region I is slightly decreased, indicating a more uniform distribution of Cu in Region I.

The effect of welding speed is shown in column (b) of Fig. 12. The same laser power but different welding speeds are used in these

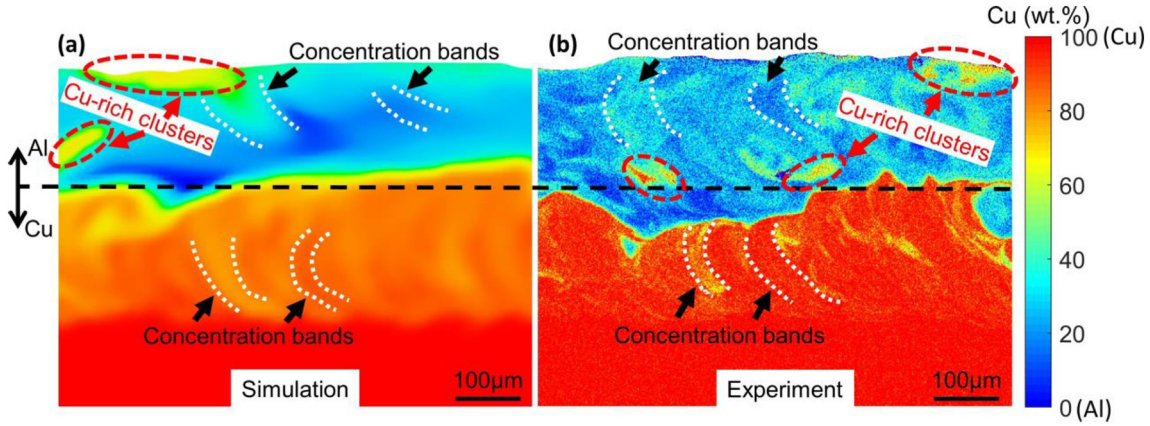

Fig. 9. Comparison between the (a) simulation result and (b) experimental result of the Cu concentration field at the longitudinal section view.

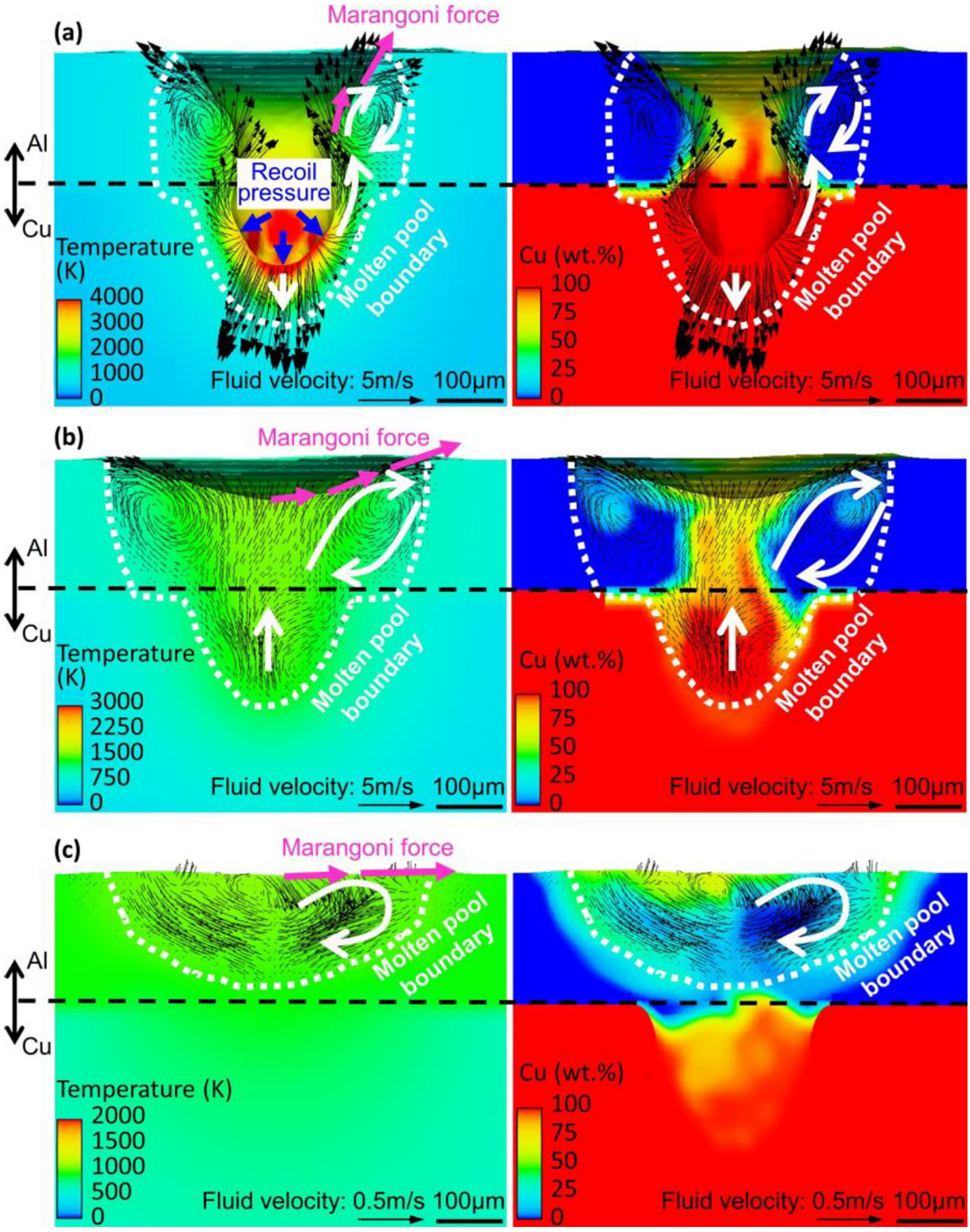

Fig. 10. Simulation results of the temperature and fluid velocity fields, and Cu concentration field of the (a) cross-section A, (b) cross-section B, and (c) cross-section C in case #6.

three cases. Due to the identical laser power, their maximum Marangoni stresses are all around 7.5×10^4 N/m^2, and their maximum fluid velocities on the molten pool surface are all around 2.6 m/s. However, the increasing welding speed causes the molten pool lifetime to decrease from 4.2 ms to 3.0 ms and 2.4 ms, which allows less time for the Marangoni-driven vortices to mix the Cu with Al. As a result, the standard deviation of Cu concentration in Region I increases from 14.5 wt% to 17.6 wt% and 19 wt%, indicating a slightly less uniform distribution of Cu.

The effects of different parameter combinations for the same heat input are shown in column (c) of Fig. 12. The welding parameters are changed from the "low" combination to the "medium" and "high" combinations in cases #1, #4, and #6. Due to the increasing laser power, the maximum Marangoni stress increases from 4.2×10^4 N/m^2 to

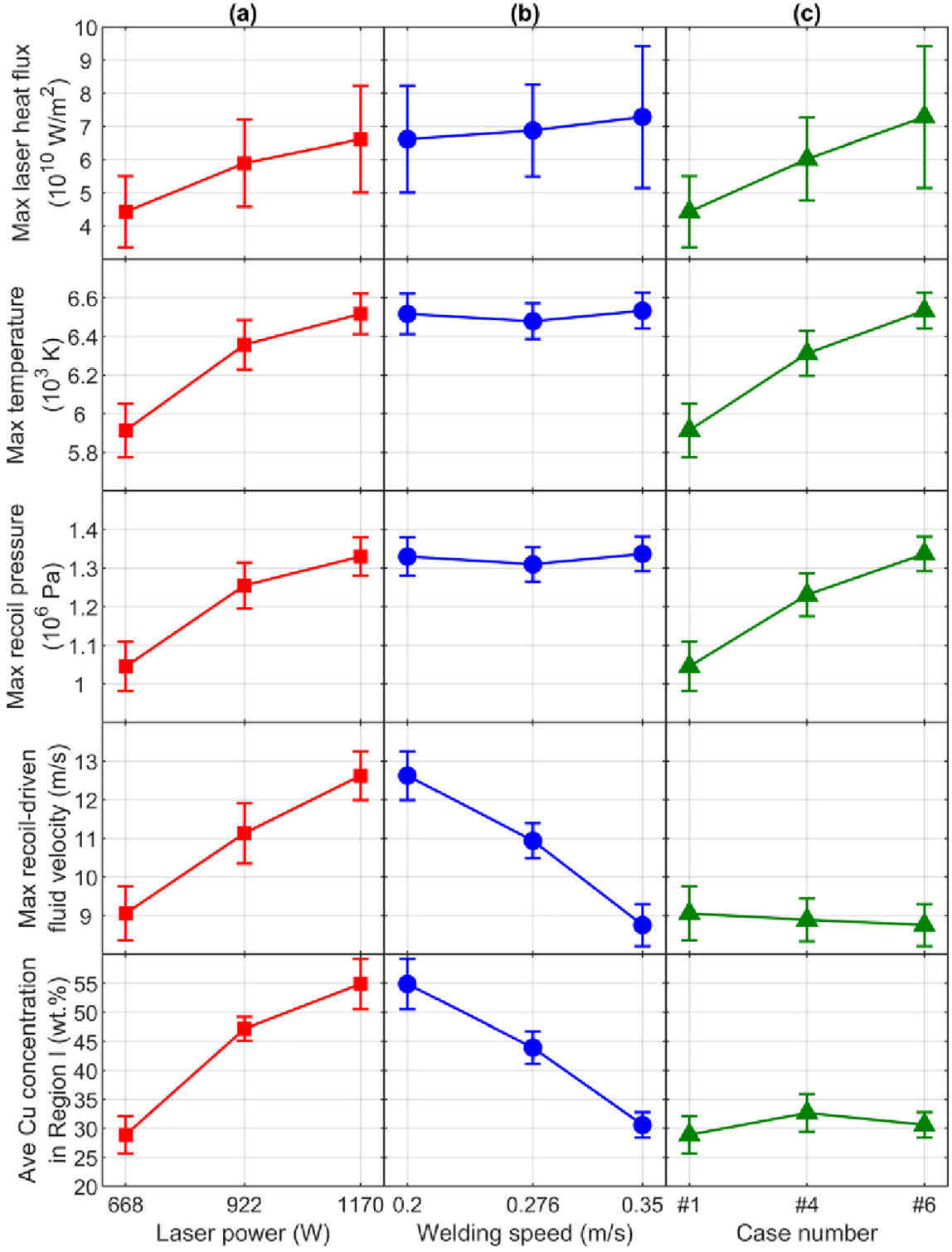

Fig. 11. Effects of welding parameters on the maximum laser heat flux, maximum temperature, maximum recoil pressure, maximum recoil-driven fluid velocity, and average Cu concentration in Region I based on the simulation result.

7×10^4 N/m^2 and 7.7×10^4 N/m^2 and the maximum surface fluid velocity is increased from 2.05 m/s to 2.35 m/s and 2.48 m/s. Due to the increasing welding speed, the molten pool lifetime is decreased from 2.8 ms to 2.6 ms and 2.4 ms. The standard deviation of the Cu concentration is found to be increasing in the three cases, indicating that the "high" parameter combination produces the least uniform Cu distribution in Region I.

5. Conclusions

In conclusion, a combination of a multi-physics numerical model and experiments are presented to understand the metal mixing process in laser keyhole welding of Al-on-Cu lap joints. On the experimental side, *ex-situ* EDS element mapping provides observations of the molten pool geometry and Cu concentration field as functions

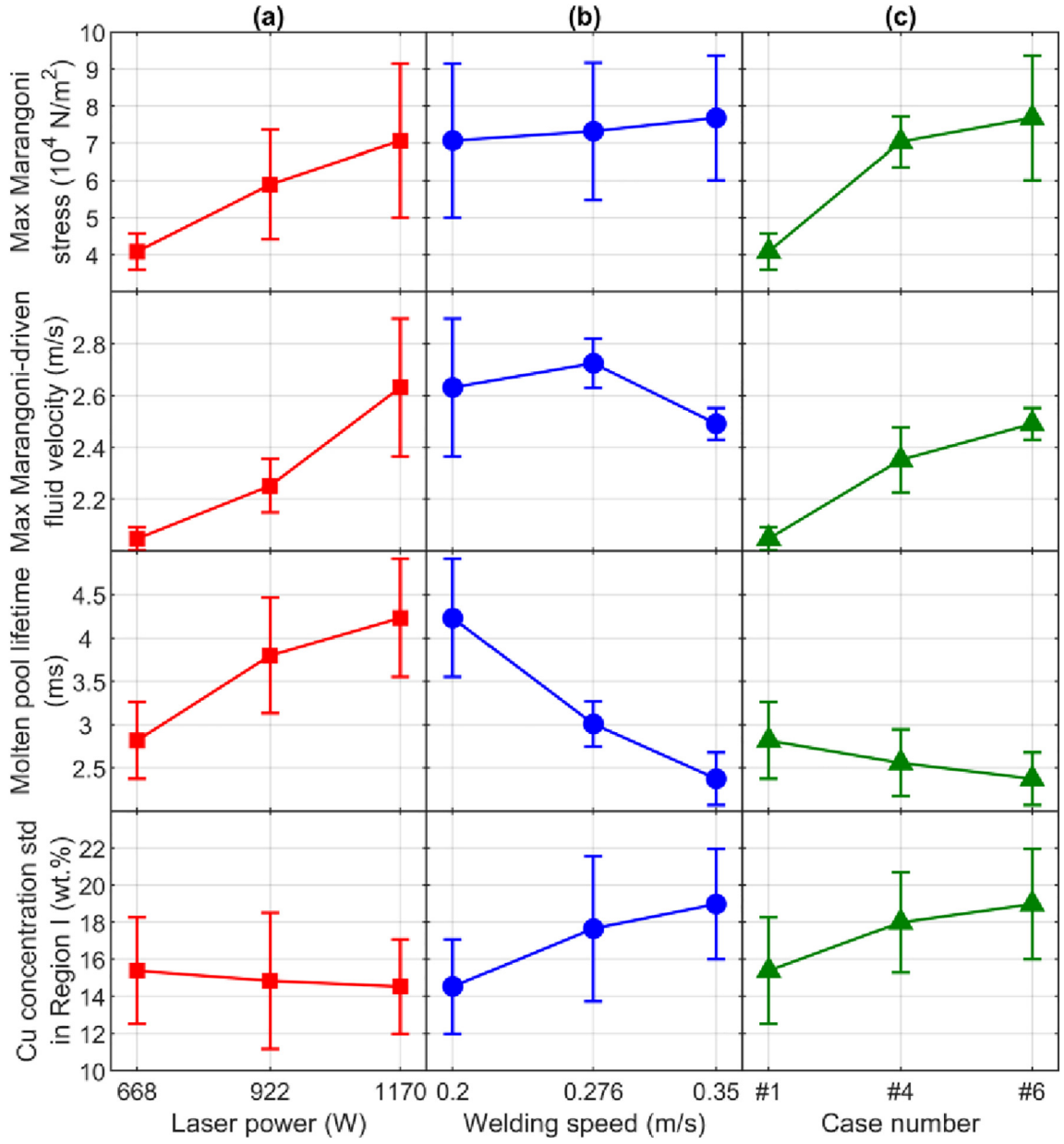

Fig. 12. Effects of welding parameters on the maximum Marangoni stress, maximum Marangoni-driven fluid velocity, molten pool lifetime, and standard deviation of Cu concentration in Region I based on the simulation result.

of laser welding parameters. On the modeling side, the numerical model successfully reproduces the molten pool geometry observed by the optical microscope and Cu concentration field observed by the EDS element mapping under different welding conditions. Moreover, the model provides information regarding the distribution of the laser heat flux on the keyhole wall and its effects on the temperature, recoil pressure, Marangoni stress, fluid flow, and metal mixing, all of which are difficult to measure via experiments. With the combination of experimental and numerical results, the major findings of the work are summarized below:

- As the laser power is increased or welding speed is decreased, the heat input is increased. This leads to larger dimensions of the molten pool, and it also allows more Cu to migrate to the top of the molten pool and mix with Al. When the heat input is fixed, the parameter combination with high laser power and high welding speed allows larger molten pool dimensions and more Cu travel upward to mix with Al. When the Cu concentration is above 50 wt% in the top region of the molten pool, cracks can be found in the fusion zone.
- The migration of Cu is due to the upward flow inside the molten pool right behind the rear keyhole wall, which is driven by the recoil pressure on the lower portion of the keyhole wall. As the laser power is increased, the keyhole wall temperature and the associated recoil pressure increase. As the welding speed is increased, less laser heating time is available for the liquid in one region to be accelerated by the recoil pressure. These two effects by the laser power and welding speed collaboratively determine the velocity of the upward flow, which positively correlates to the amount of Cu that can migrate to the top region of the molten pool.
- The Al—Cu mixing in the top region of the molten pool is enabled by the vortices on the two sides of the molten pool near its top surface. The vortices are primarily driven by the Marangoni force on the molten pool surface. As the laser power is increased, the Marangoni force increases, which helps to accelerate the vortices and mix Cu with Al

more effectively. As the welding speed is increased, less time is available for the vortices to mix Cu and Al in the molten pool. These two effects collaboratively determine the uniformity of the Al—Cu mixing in the top region of the molten pool.
- While the fluid flow and metal mixing in laser keyhole welding follow the above general patterns, the fluid velocity and the uniformity of metal mixing both vary in space and time due to the intrinsic fluctuation of the keyhole.

The combination of experiments and numerical modeling provides an effective approach to understand the complex phenomena of the fluid flow and metal mixing process in laser keyhole welding of dissimilar metals. This framework is expected to provide insights regarding the IMC formation during the molten pool solidification, which is critical for the properties and performance of the joints between dissimilar metals.

Data availability

The raw/processed data required to reproduce these findings cannot be shared at this time as the data also forms part of an ongoing study.

Author contribution

Wenkang Huang: software, validation, investigation, formal analysis, writing - original draft.

Hongliang Wang: conceptualization, resources, supervision, writing – review & editing.

Teresa Tinker: software, writing – review & editing.

Wenda Tan: conceptualization, supervision, writing – review & editing.

Declaration of Competing Interest

The authors declare that they have no known competing financial interests or personal relationships that could have appeared to influence the work reported in this paper.

Acknowledgments

The authors wish to gratefully acknowledge the partial financial support provided by the National Science Foundation under Grant No. CMMI-1752218. This work made use of the University of Utah USTAR shared facilities supported, in part, by the MRSEC Program of the National Science Foundation under Award No. DMR-1121252. The authors also would like to thank Diana Wegner (Staff Researcher at General Motors), David Souders (Vice President of Support and Services at Flow Science), and Dr. Nannan Chen (Postdoctoral Researcher at Pennsylvania State University) for their help throughout this study.

References

[1] H. Wang, S. Wagner, R. Sekol, N. Chen, T. Perry, J. Schroth, Resistive joining – a novel dissimilar welding method for thin sheet metals, Procedia Manuf. 48 (2020) 141–146, https://doi.org/10.1016/j.promfg.2020.05.030.

[2] P. Cavaliere, R. Nobile, F.W. Panella, A. Squillace, Mechanical and microstructural behaviour of 2024-7075 aluminium alloy sheets joined by friction stir welding, Int. J. Mach. Tools Manuf. 46 (2006) 588–594, https://doi.org/10.1016/j.ijmachtools.2005.07.010.

[3] T. Dursun, C. Soutis, Recent developments in advanced aircraft aluminium alloys, Mater. Des. 56 (2014) 862–871, https://doi.org/10.1016/j.matdes.2013.12.002.

[4] R. Yuan, S. Deng, H. Cui, Y. Chen, F. Lu, Interface characterization and mechanical properties of dual beam laser welding-brazing Al/steel dissimilar metals, J. Manuf. Process. 40 (2019) 37–45, https://doi.org/10.1016/j.jmapro.2019.03.005.

[5] P. Li, Z. Lei, X. Zhang, J. Liu, Y. Chen, Effects of laser power on the interfacial intermetallic compounds and mechanical properties of dual-spot laser welded–brazed Ti/Al butt joint, Opt. Laser Technol. 124 (2020) 105987, https://doi.org/10.1016/j.optlastec.2019.105987.

[6] S. Chen, G. Yu, S. Li, J. Yang, J. Huang, S. Chen, Interfacial microstructures and mechanical property of Ni/Al dissimilar butt joint made by laser welding, J. Manuf. Process. 50 (2020) 17–23, https://doi.org/10.1016/j.jmapro.2019.12.026.

[7] A. Jain, P. Sonia, S. Kumari, P. Pushp, Study of intermetallic compound (IMC) formed in welding of steel with magnesium: a review, Mater. Today Proc. 26 (2020) 1159–1166, https://doi.org/10.1016/j.matpr.2020.02.232.

[8] T. Solchenbach, P. Plapper, W. Cai, Electrical performance of laser braze-welded aluminum–copper interconnects, J. Manuf. Process. 16 (2014) 183–189, https://doi.org/10.1016/j.jmapro.2013.12.002.

[9] T. Solchenbach, P. Plapper, Mechanical characteristics of laser braze-welded aluminium-copper connections, Opt. Laser Technol. 54 (2013) 249–256, https://doi.org/10.1016/j.optlastec.2013.06.003.

[10] P. Schmalen, P. Plapper, W. Cai, Process robustness of laser braze-welded Al/Cu connectors, SAE Int. J. Altern. Powertrains. 5 (2016) 195–204, https://doi.org/10.4271/2016-01-1198.

[11] L. Zhou, Z.Y. Li, X.G. Song, C.W. Tan, Z.Z. He, Y.X. Huang, J.C. Feng, Influence of laser offset on laser welding-brazing of Al/brass dissimilar alloys, J. Alloys Compd. 717 (2017) 78–92, https://doi.org/10.1016/j.jallcom.2017.05.099.

[12] D. Narsimhachary, K. Dutta, S.M. Shariff, G. Padmanabham, A. Basu, Mechanical and microstructural characterization of laser weld-brazed AA6082-galvanized steel joint, J. Mater. Process. Technol. 263 (2019) 21–32, https://doi.org/10.1016/j.jmatprotec.2018.08.002.

[13] Y. Zhang, D.Q. Sun, X.Y. Gu, H.M. Li, Nd:YAG pulsed laser welding of dissimilar metals of titanium alloy to stainless steel, Int. J. Adv. Manuf. Technol. 94 (2018) 1073–1085, https://doi.org/10.1007/s00170-017-0997-3.

[14] L. Chen, C. Wang, L. Xiong, X. Zhang, G. Mi, Microstructural, porosity and mechanical properties of lap joint laser welding for 5182 and 6061 dissimilar aluminum alloys under different place configurations, Mater. Des. 191 (2020) 108625, https://doi.org/10.1016/j.matdes.2020.108625.

[15] S. Guo, Y. Peng, C. Cui, Q. Gao, Q. Zhou, J. Zhu, Microstructure and mechanical characterization of re-melted Ti-6Al-4V and Al-Mg-Si alloys butt weld, Vacuum. 154 (2018) 58–67, https://doi.org/10.1016/j.vacuum.2018.04.048.

[16] A. Fortunato, A. Ascari, Laser welding of thin copper and aluminum sheets: feasibility and challenges in continuous-wave welding of dissimilar metals, Lasers Manuf. Mater. Process. 6 (2019) 136–157, https://doi.org/10.1007/s40516-019-00085-z.

[17] A. Shamsolhodaei, Q. Sun, X. Wang, B. Panton, H. Di, Y.N. Zhou, Effect of laser positioning on the microstructure and properties of NiTi-copper dissimilar laser welds, J. Mater. Eng. Perform. 29 (2020) 849–857, https://doi.org/10.1007/s11665-020-04637-9.

[18] Z. Jiang, X. Chen, K. Yu, Z. Lei, Y. Chen, S. Wu, Z. Li, Improving fusion zone microstructure inhomogeneity in dissimilar-metal welding by laser welding with oscillation, Mater. Lett. 261 (2020) 126995, https://doi.org/10.1016/j.matlet.2019.126995.

[19] M. Kraetzsch, J. Standfuss, A. Klotzbach, J. Kaspar, B. Brenner, E. Beyer, Laser beam welding with high-frequency beam oscillation: welding of dissimilar materials with brilliant fiber lasers, Phys. Procedia 12 (2011) 142–149, https://doi.org/10.1016/j.phpro.2011.03.018.

[20] L. Wang, M. Gao, Z. Hao, A pathway to mitigate macrosegregation of laser-arc hybrid Al-Si welds through beam oscillation, Int. J. Heat Mass Transf. 151 (2020) 119467, https://doi.org/10.1016/j.ijheatmasstransfer.2020.119467.

[21] A.K. Gilmutdinov, A.I. Gorunov, O.A. Nyukhlaev, M. Schmidt, Investigations of the sound frequency effect on laser acoustic welding of stainless steel, Int. J. Adv. Manuf. Technol. 106 (2020) 3033–3043, https://doi.org/10.1007/s00170-019-04825-5.

[22] S. Zhou, G. Ma, W. Dongjiang, D. Chai, M. Lei, Ultrasonic vibration assisted laser welding of nickel-based alloy and austenite stainless steel, J. Manuf. Process. 31 (2018) 759–767, https://doi.org/10.1016/j.jmapro.2017.12.023.

[23] Z. Zhu, K.Y. Lee, X. Wang, Ultrasonic welding of dissimilar metals, AA6061 and Ti6Al4V, Int. J. Adv. Manuf. Technol. 59 (2012) 569–574, https://doi.org/10.1007/s00170-011-3534-9.

[24] F. Yan, X. Wang, F. Chai, H. Ma, L. Tian, X. Du, C. Wang, W. Wang, Improvement of microstructure and performance for steel/Al welds produced by magnetic field assisted laser welding, Opt. Laser Technol. 113 (2019) 164–170, https://doi.org/10.1016/j.optlastec.2018.12.030.

[25] H. Ding, J. Xu, W. Tan, S. Huang, J. Zhou, Influence of magnetic field on properties of Fe/Al dissimilar metal laser welding joints, Zhongguo Jiguang/Chinese J. Lasers. 44 (2017), 0902003 https://doi.org/10.3788/CJL201744.0902003.

[26] Y. Liu, Q. Sun, J. Liu, S. Wang, J. Feng, Effect of axial external magnetic field on cold metal transfer welds of aluminum alloy and stainless steel, Mater. Lett. 152 (2015) 29–31, https://doi.org/10.1016/j.matlet.2015.03.077.

[27] G. Phanikumar, K. Chattopadhyay, P. Dutta, Modelling of transport phenomena in laser welding of dissimilar metals, Int. J. Numer. Methods Heat Fluid Flow. 11 (2001) 156–171, https://doi.org/10.1108/09615530110381575.

[28] G. Phanikumar, P. Dutta, K. Chattopadhyay, Computational modeling of laser welding of Cu-Ni dissimilar couple, Metall. Mater. Trans. B Process Metall. Mater. Process. Sci. 35 (2004) 339–350, https://doi.org/10.1007/s11663-004-0034-4.

[29] Y. Hu, X. He, G. Yu, Z. Ge, C. Zheng, W. Ning, Heat and mass transfer in laser dissimilar welding of stainless steel and nickel, Appl. Surf. Sci. 258 (2012) 5914–5922, https://doi.org/10.1016/j.apsusc.2012.02.143.

[30] M.R.N. Esfahani, J. Coupland, S. Marimuthu, Numerical simulation of alloy composition in dissimilar laser welding, J. Mater. Process. Technol. 224 (2015) 135–142, https://doi.org/10.1016/j.jmatprotec.2015.05.005.

[31] Z. Xue, S. Hu, D. Zuo, W. Cai, D. Lee, K.A. Elijah, Molten pool characterization of laser lap welded copper and aluminum, J. Phys. D. Appl. Phys. 46 (2013) 495501, https://doi.org/10.1088/0022-3727/46/49/495501.

[32] A. De, T. DebRoy, A smart model to estimate effective thermal conductivity and viscosity in the weld pool, J. Appl. Phys. 95 (2004) 5230–5240, https://doi.org/10.1063/1.1695593.
[33] R. Rai, S.M. Kelly, R.P. Martukanitz, T. DebRoy, A convective heat-transfer model for partial and full penetration keyhole mode laser welding of a structural steel, Metall. Mater. Trans. A Phys. Metall. Mater. Sci. 39 (2008) 98–112, https://doi.org/10.1007/s11661-007-9400-6.
[34] N. Chakraborty, S. Chakraborty, Modelling of turbulent molten pool convection in laser welding of a copper-nickel dissimilar couple, Int. J. Heat Mass Transf. 50 (2007) 1805–1822, https://doi.org/10.1016/j.ijheatmasstransfer.2006.10.030.
[35] N. Chakraborty, The effects of turbulence on molten pool transport during melting and solidification processes in continuous conduction mode laser welding of copper-nickel dissimilar couple, Appl. Therm. Eng. 29 (2009) 3618–3631, https://doi.org/10.1016/j.applthermaleng.2009.06.018.
[36] A. Matsunawa, J.-D. Kim, N. Seto, M. Mizutani, S. Katayama, Dynamics of keyhole and molten pool in laser welding, J. Laser Appl. 10 (1998) 247–254, https://doi.org/10.2351/1.521858.
[37] R. Cunningham, C. Zhao, N. Parab, C. Kantzos, J. Pauza, K. Fezzaa, T. Sun, A.D. Rollett, Keyhole threshold and morphology in laser melting revealed by ultrahigh-speed x-ray imaging, Science. 363 (2019) 849–852, https://doi.org/10.1126/science.aav4687.
[38] N. Kouraytem, X. Li, R. Cunningham, C. Zhao, N. Parab, T. Sun, A.D. Rollett, A.D. Spear, W. Tan, Effect of laser-matter interaction on molten pool flow and keyhole dynamics, Phys. Rev. Appl. 11 (2019), 064054https://doi.org/10.1103/PhysRevApplied.11.064054.
[39] J. Peng, L. Li, S. Lin, F. Zhang, Q. Pan, S. Katayama, High-speed X-ray transmission and numerical study of melt flows inside the molten pool during laser welding of aluminum alloy, Math. Probl. Eng. 2016 (2016) 1409872, https://doi.org/10.1155/2016/1409872.
[40] S. Pang, L. Chen, J. Zhou, Y. Yin, T. Chen, A three-dimensional sharp interface model for self-consistent keyhole and weld pool dynamics in deep penetration laser welding, J. Phys. D. Appl. Phys. 44 (2011) 25301, https://doi.org/10.1088/0022-3727/44/2/025301.
[41] H. Ki, P.S. Mohanty, J. Mazumder, Modeling of laser keyhole welding: Part I. Mathematical modeling, numerical methodology, role of recoil pressure, multiple reflections, and free surface evolution, Metall. Mater. Trans. A Phys. Metall. Mater. Sci. 33 (2002) 1817–1830, https://doi.org/10.1007/s11661-002-0190-6.
[42] S. Zhao, G. Yu, X. He, Y. Zhang, W. Ning, Numerical simulation and experimental investigation of laser overlap welding of Ti6Al4V and 42CrMo, J. Mater. Process. Technol. 211 (2011) 530–537, https://doi.org/10.1016/j.jmatprotec.2010.11.007.
[43] J. Ma, F. Kong, R. Kovacevic, Finite-element thermal analysis of laser welding of galvanized high-strength steel in a zero-gap lap joint configuration and its experimental verification, Mater. Des. 36 (2012) 348–358, https://doi.org/10.1016/j.matdes.2011.11.027.
[44] G.A. Moraitis, G.N. Labeas, Residual stress and distortion calculation of laser beam welding for aluminum lap joints, J. Mater. Process. Technol. 198 (2008) 260–269, https://doi.org/10.1016/j.jmatprotec.2007.07.013.
[45] H. Koch, K. Leitz, A. Otto, M. Schmidt, Process analysis of laser beam welding steel sheets in overlap configuration by using a 3d transient simulation model, Proc. Fifth Int. WLT-Conference Lasers Manuf. 2009, pp. 777–782 https://www.researchgate.net/publication/285323558.
[46] C. Wang, B. Lei, P. Jiang, X. Xu, G. Mi, Numerical and experimental investigation of vacuum-assisted laser welding for DP590 galvanized steel lap joint without prescribed gap, Int. J. Adv. Manuf. Technol. 94 (2018) 4177–4185, https://doi.org/10.1007/s00170-017-1067-6.
[47] V.I. Isaev, A.N. Cherepanov, V.P. Shapeev, Numerical study of heat modes of laser welding of dissimilar metals with an intermediate insert, Int. J. Heat Mass Transf. 99 (2016) 711–720, https://doi.org/10.1016/j.ijheatmasstransfer.2016.04.019.
[48] I. Tomashchuk, P. Sallamand, J.M. Jouvard, The modeling of dissimilar welding of immiscible materials by using a phase field method, Appl. Math. Comput. 219 (2013) 7103–7114, https://doi.org/10.1016/j.amc.2012.01.039.
[49] J. Wu, H. Zhang, Y. Feng, B.B. Luo, 3D multiphysical modelling of fluid dynamics and mass transfer in laser welding of dissimilar materials, Metals (Basel) 8 (2018) 443, https://doi.org/10.3390/met8060443.
[50] W. Tan, W. Huang, Numerical modeling of thermo-fluid flow and metal mixing in laser keyhole welding of dissimilar metals, ASME 2018 13th Int. Manuf. Sci. Eng. Conf. MSEC 2018 (2) (2018)https://doi.org/10.1115/MSEC2018-6640V002T04A043.
[51] M. Leitner, T. Leitner, A. Schmon, K. Aziz, G. Pottlacher, Thermophysical properties of liquid aluminum, Metall. Mater. Trans. A. 48 (2017) 3036–3045, https://doi.org/10.1007/s11661-017-4053-6.
[52] D.A. Harrison, D. Yan, S. Blairs, The surface tension of liquid copper, J. Chem. Thermodyn. 9 (1977) 1111–1119, https://doi.org/10.1016/0021-9614(77)90112-4.
[53] M.J. Assael, A.E. Kalyva, K.D. Antoniadis, R. Michael Banish, I. Egry, J. Wu, E. Kaschnitz, W.A. Wakeham, Reference data for the density and viscosity of liquid copper and liquid tin, J. Phys. Chem. Ref. Data 39 (2010), 033105 https://doi.org/10.1063/1.3467496.
[54] C. Cagran, Thermal Conductivity and Thermal Diffusivity of Liquid Copper, Graz University of Technology, 2000 https://www.tugraz.at/fileadmin/user_upload/Institute/IEP/Thermophysics_Group/Files/DA-CagranClaus.pdf.
[55] J.Y. Lee, S.H. Ko, D.F. Farson, C.D. Yoo, Mechanism of keyhole formation and stability in stationary laser welding, J. Phys. D. Appl. Phys. 35 (2002) 1570–1576, https://doi.org/10.1088/0022-3727/35/13/320.
[56] J. Zhou, H.L. Tsai, P.C. Wang, Transfort phenomena and keyhole dynamics during pulsed laser welding, J. Heat Transf. 128 (2006) 680–690, https://doi.org/10.1115/1.2194043.
[57] E.H. Amara, R. Fabbro, Modelling of gas jet effect on the melt pool movements during deep penetration laser welding, J. Phys. D. Appl. Phys. 41 (2008), 055503 https://doi.org/10.1088/0022-3727/41/5/055503.
[58] H. Zhao, W. Niu, B. Zhang, Y. Lei, M. Kodama, T. Ishide, Modelling of keyhole dynamics and porosity formation considering the adaptive keyhole shape and three-phase coupling during deep-penetration laser welding, J. Phys. D. Appl. Phys. 44 (2011) 485302, https://doi.org/10.1088/0022-3727/44/48/485302.
[59] V. Semak, A. Matsunawa, The role of recoil pressure in energy balance during laser materials processing, J. Phys. D. Appl. Phys. 30 (1997) 2541–2552, https://doi.org/10.1088/0022-3727/30/18/008.
[60] J.H. Cho, S.J. Na, Implementation of real-time multiple reflection and Fresnel absorption of laser beam in keyhole, J. Phys. D. Appl. Phys. 39 (2006) 5372–5378, https://doi.org/10.1088/0022-3727/39/24/039.
[61] W. Tan, N.S. Bailey, Y.C. Shin, Investigation of keyhole plume and molten pool based on a three-dimensional dynamic model with sharp interface formulation, J. Phys. D. Appl. Phys. 46 (2013), 055501https://doi.org/10.1088/0022-3727/46/5/055501.
[62] T.R. Allen, W. Huang, J.R. Tanner, W. Tan, J.M. Fraser, B.J. Simonds, Energy coupling mechanisms revealed through simultaneous keyhole depth and absorptance measurements during laser-metal processing, Phys. Rev. Appl. 13 (2020), 064070https://doi.org/10.1103/PhysRevApplied.13.064070.
[63] E. Kaiser, G. Ambrosy, E. Papastathopoulos, Welding strategies for joining copper and aluminum by fast oscillating, high quality laser beam, Proc. SPIE 11273, High-Power Laser Mater. Process. Appl. Diagnostics, Syst. IX 2020, p. 112730C, https://doi.org/10.1117/12.2545893.